IEEE Access
Multidisciplinary ⋮ Rapid Review ⋮ Open Access Journal

Received March 16, 2022, accepted April 2, 2022, date of publication April 11, 2022, date of current version April 15, 2022.

Digital Object Identifier 10.1109/ACCESS.2022.3166263

Compensation of Aerodynamic Sampling Effects of a Cloud Droplet Instrument

HARRI J. JUTTULA[1], VILLE A. KAIKKONEN[1], EERO O. MOLKOSELKÄ[2], AND ANSSI J. MÄKYNEN[2]

[1]Unit of Measurement Technology, University of Oulu, 90014 Kajaani, Finland
[2]Optoelectronics and Measurement Techniques Laboratory, University of Oulu, 90014 Oulu, Finland

Corresponding author: Harri J. Juttula (harri.juttula@oulu.fi)

This work was supported in part by the European Regional Development Fund (ERDF) under European Territorial Cooperation (ETC) program Interreg V A Nord under Grant NYPS 20202472, and in part by the Regional Council of Lapland under Grant 126/00.01.05.24.02/2019.

ABSTRACT Precise sampling is a crucial part of the aerosol measurement processes that ideally requires perfectly isokinetic conditions in which particles in the sampling volume move exactly the same way as they would in an undisturbed flow. Such conditions might be difficult to achieve in practical measurement situations where the direction and speed of the air stream may change continuously. We propose a novel method avoiding sampling errors due to moderately disturbed particle flow in case of an imaging cloud droplet instrument. It is shown that despite the non-isokinetic and non-isoaxial conditions accurate droplet density can be obtained by rejecting part of the measurement volume in post processing. The adjustment of the sampling volume is easily applied using a holographic imaging method, which offers multiple well-defined image planes to accurately set the boundaries of the sampling volume. To verify the hypothesis, aerodynamic sampling effects of a holographic cloud droplet instrument are studied using computational fluid dynamics (CFD) and particle tracing simulations and by comparing them with wind tunnel experiments. We found out that changes in the airflow affected the particle density mostly near the walls of the probe. It was observed that the error in droplet density could be kept under 10 % by limiting the cross-channel depth of the measurement volume to two-thirds of the full wall-to-wall distance. Further improvement was achieved by using simulation results to formulate a relation between sampled and ambient droplet concentration as a function of droplet diameter and air speed. Less than 1 % deviation in droplet density was achieved in this case compared to simulated values. Orientation of the instrument's inlet relative to the direction of airflow was found out to have the strongest effect on the achievable accuracy. Results show that the droplets can be reliably sampled also in a non-isoaxial case if the measurement volume was further reduced. Reasonable accuracy was achieved with 10-degree deviation within limited air speed and droplet diameter range.

INDEX TERMS Calibration, cloud droplets, computational fluid dynamics, digital holography, environmental measurements, icing, isokinetic sampling, particle tracing.

I. INTRODUCTION

Accurate knowledge of cloud droplet statistics is important for describing the microphysical properties of clouds [1], [2] or atmospheric icing of structures [3]. Macroscopic properties of clouds are derived from the individual droplets and they play an important role in modern climate models. Icing is a more concrete example of interaction with a cloud droplets which is related to liquid water content (LWC) and median volume diameter (MVD) of the clouds. Cold climate regions or high altitude locations are especially susceptible to icing and problems related to it. For example, icing changes the properties of wind turbine blades and leads to production and financial losses [4]–[6]. Besides the temperature and air speed the LWC of the air and the MVD of the supercooled cloud droplets are the most important parameters determining the severity of icing conditions. Both LWC and MVD can be calculated from the droplet size distribution but their measurement is challenging due to the wide range of possible cloud droplet and raindrop sizes (1 μm to 10 mm) and number concentrations (10^{-5} to 10^{3} cm^{-3}) in the air.

The associate editor coordinating the review of this manuscript and approving it for publication was Giambattista Gruosso.

Several instruments to measure these parameters with different measurement principles have been developed over the years and a lot of work has been done for their intercomparison. Common measurement principles include, for example, forward scattering methods [7], [8], 2D shadow imaging [9]–[12], phase Doppler interferometry [13], [14] and holography [15]–[17] with each method having their own strengths and weaknesses. Regardless of the measurement principle, however, a common challenge for all instruments is the undisturbed sampling of the airflow. The physical shape of the instrument itself affects the airflow which again will affect the density and size distribution of the particles in the sampling volume. While the effects of disturbed airflow are rarely discussed, some studies have raised concerns related to sampling in different wind speed and direction conditions [12], [18], [19]. Besides this sample volume contamination by the impact shattering of droplets has also been recognized as one of the main error sources related to sampling [20].

Ideally, a cloud droplet measurement should sample the airflow isokinetically and isoaxially or a compensation method for non-ideal conditions should be implemented. Isokinetic sampling means that the inlet flow velocity v of the instrument is equal to the ambient flow velocity v_0 while isoaxial sampling means that the inlet flow direction matches the ambient wind direction. Changes in the wind speed and direction are typical causes for the sampling uncertainty of cloud droplet instruments. If probe design doesn't satisfy the isokinetic sampling condition, a correction algorithm based on theory or calibration measurements should be used. In both cases the correction should take into account both droplet size and wind speed. Isoaxial measurement conditions can be ensured by rotationally symmetric design or with a rotating installation. If neither is implemented in the design, only measurements with matching wind direction should be considered reliable.

In our previous work [21] our assumption was that the instrument would be continuously aligned with the wind. In practice small deviations from the wind direction are common due to fast changes in wind direction and the rotational inertia of the instrument. We also propose a novel method to compensate the sampling errors due to the misalignment of airflow by adjusting the position and size of the sampled volume inside the particle flow of the probe.

In this work we have studied the isokinetic sampling of our rotating cloud droplet instrument with computational fluid dynamics (CFD). We used the CFD simulations to solve the airflow through the instrument and then used particle tracing based on the drag forces acting on different droplet sizes to study the sampling effects in different wind conditions. The instrument studied here is capable of detecting the size and 3D position of the cloud droplets passing through its sample volume, which allows a direct comparison with the simulations. Simulation results were compared against real measurement data from controlled wind tunnel experiments. Both wind tunnel measurements and CFD simulations are in good agreement and they reveal aerodynamic sampling effects that depend on droplet size, wind speed and direction. The results reveal a new beneficial property of holographic droplet imaging instruments which allows easy and dynamic optimization of the sampling volume to avoid sampling errors.

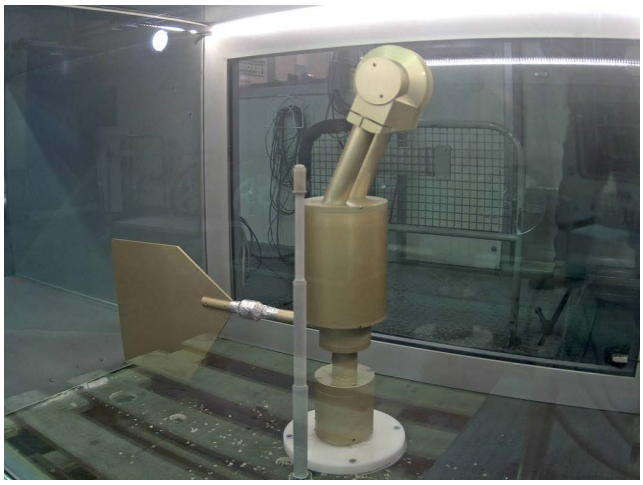

FIGURE 1. A photograph of the cloud droplet instrument in a wind tunnel with icing conditions. Measurement volume is located at the center of two symmetrical arms at the top of the instrument body. Airflow is directed between the arms by conical knife-edge air guides.

II. MATERIALS AND METHODS

A. CLOUD DROPLET INSTRUMENT

Structure of the droplet instrument consists of a cylindrical body, tail and two identical arms with sharp conical air guides. The instrument is shown in Fig. 1 installed in a wind tunnel. First instrument arm contains a laser illumination source while the second arm contains an image sensor. Both the laser and the image sensor are behind protective glass windows. The inner surfaces of the instrument contain multiple heating elements for the anti-icing of the outer surface of the instrument. Instrument body houses the control unit and external communications and is connected to a pole with a freely rotating axle which allows the tail to orient the instrument arms in a direction of the wind.

The pulsed laser source illuminates the cloud droplets flowing between the arms and the image sensor captures the resulting interference pattern (hologram). Shadow images of the droplets within the sample volume are then reconstructed from the hologram. The size and position parameters are obtained from the reconstructed droplet images. Details of the holographic measurement principle and the cloud droplet instrument are described in our previous works [21]–[24]. One advantage of the holographic imaging system is that it provides the 3D information about individual droplets in post processing which makes it possible to dynamically adjust the measurement volume within the illuminated volume [25]. This property allows us to reject droplets that are too close or on the surface of the instrument walls that limit the maximum length of the measurement volume to 30 mm. Minimum and maximum distance of the accepted droplets from the

image sensor can be thus adjusted with better than 50 micron accuracy which is the longitudinal resolution of the cloud droplet instrument.

Overall prototype design shown in Fig. 1 is a result of an ad hoc process to design a simple rotating instrument that can withstand strong winds and icing conditions. Sharp knife-edge air guides were added to the design for better airflow and protection from shattered droplets. CFD simulations were used during prototyping to adjust arm lengths and angles to minimize changes to the wind speed and direction entering the imaging volume between the arms. The separation of the air guides is 30 mm and their diameter is 100 mm.

B. CFD AND DROPLET TRACING SIMULATIONS

We used COMSOL Multiphysics 5.4 to perform numerical CFD and droplet tracing simulations. Wind speeds and droplet sizes were chosen to cover the typical wind and icing conditions for a stationary installation of the cloud droplet instrument. While the instrument is able to align itself to the wind, non-zero angles of attack were also taken into consideration to examine the non-isoaxial performance of the instrument. In practice, we first calculated a stationary CFD solution for all combinations of wind speed and angle of attack and then used the solution to calculate the drag force acting on the droplets. Droplet paths were then calculated and droplet density in the measurement volume of the instrument was recorded.

We assumed the CFD simulations to be independent of the droplet tracing and solved first the velocity vector field. The stationary solution of the airflow was later used as an input to the droplet tracing. We used COMSOL to solve the air velocity field with the Reynolds-averaged Navier-Stokes equations using the k-ϵ turbulent flow model [26].

$$\rho\frac{\partial \mathbf{u}}{\partial t} + \rho(\mathbf{u}\cdot\nabla)\mathbf{u} = \nabla\cdot[-p\mathbf{I} + \boldsymbol{\kappa}] + \mathbf{F} \quad (1)$$

$$\rho(\nabla\cdot\mathbf{u}) = 0 \quad (2)$$

Here ρ, p and $\mathbf{u}$ are the density, pressure and velocity vector of the air respectively, $\mathbf{F}$ is the force acting on a volume and $\mathbf{I}$ is the identity tensor. Viscous stress tensor $\boldsymbol{\kappa}$ and turbulent viscosity μ_T used in k-ϵ turbulent flow model can be written as:

$$\boldsymbol{\kappa} = (\mu + \mu_T)(\nabla\mathbf{u} + (\nabla\mathbf{u})^T) \quad (3)$$

$$\mu_T = \rho C_\mu k^2/\epsilon \quad (4)$$

where μ is the dynamic viscosity of the medium, C_μ is a constant and k and ϵ are the turbulent kinetic energy and dissipation rate respectively.

After solving the velocity vector field $\mathbf{u}$ particle tracing can be done by calculating the Stokes drag force acting on the droplets with mass m [27].

$$\mathbf{F_D} = \frac{1}{\tau_p} m(\mathbf{u} - \mathbf{v}) \quad (5)$$

where τ_p is the particle velocity response time, $\mathbf{u}$ is the air velocity and $\mathbf{v}$ is the particle velocity. With the Stokes drag law particle velocity response time for spherical droplets can be written as $\tau_p = \rho_p d_p^2/18\mu$ where ρ_p and d_p are the droplet density and diameter.

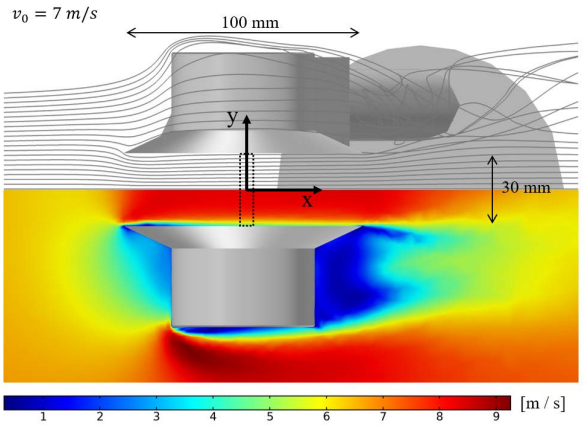

FIGURE 2. A top-down view of the 3D simulation model of the cloud droplet instrument with an initial wind speed of 7 m/s. Streamlines and air velocity around the instrument are illustrated. The measurement volume of the instrument is shown with a dashed rectangle.

In practice, we used COMSOL to create a model of air volume surrounding a 3D model of the instrument shown in Fig. 1. The simulated air volume was a cylinder which axis of symmetry is the x-axis shown in Fig. 2. The radius of the air cylinder was 0.5 m and its axis extended 0.6 meters upstream and 1.8 meters downstream from the origin. Air volume was meshed with COMSOL's adaptive meshing algorithm with mirror symmetry about the xz-plane. A boundary layer mesh with a dense element distribution along instrument walls was used. Elsewhere COMSOL used free tetrahedral meshing. Compressible flow and no slip boundary condition options were used. In particle tracing calculations droplets were assumed to be independent of each other and they were terminated if they collided with instrument walls.

A mesh independence test was performed by computing the velocity and pressure solution for $v_0 = 10$ m/s case on successively finer meshes ranging from approximately 0.3 million to 3.3 million volume elements. Solutions converged above 1.1 million elements and velocity stayed within $\pm 1\%$ from the solution with the finest mesh. Mesh with 1.6 million elements was chosen for calculations.

III. RESULTS

A. COORDINATE SYSTEM

All the results are presented in the same global coordinates that were used in the simulations. Origin of the coordinate system is shown in Fig. 2 and it is located at the center of the measurement volume of the instrument. Measurement volume is limited in y-direction by the instrument arms walls which are at 15 mm distance from the origin. Wind direction is in the direction of the positive x-axis and the angle of attack is measured from the x-axis in xy-plane.

B. SIMULATED AIRFLOW

Stationary CFD solution was calculated for all combinations of wind speeds of 5, 10, 20 and 40 m/s and angles of attack

of 0, 5, 10 and 15 degrees. Additionally 7 m/s wind speed was simulated with 0° angle of attack to match the conditions of a wind tunnel test for comparison.

Results of the CFD simulations for 0° angle of attack are illustrated in Fig. 2 and Fig. 3. From these figure it can be seen that the flow experiences changes in its direction and velocity when going through the instrument while the relative flow speed v/v_0 is almost independent of the ambient wind speed v_0. In each case, the wind speed drops to $0.87v_0$ before the instrument and then accelerates to approximately $1.18v_0$ when air flows through the instrument as shown in Fig. 3. By definition it is clear that the flow through the instrument is not isokinetic since the flow experiences directional changes and $v/v_0 \neq 1$. No significant changes in the z component of the wind speed were observed. Knife-edged air guides slice the airflow before it is deflected around the instrument and the flow is not disturbed inside the sample volume. Only observed changes inside the sample volume were the acceleration of wind speed in the center and a rapid drop in wind speed near the instrument walls as seen in Fig. 3. In $\theta > 0°$ cases the flow redirected parallel to instrument walls inside the sample volume and overall acceleration was again observed but the relative speed v/v_0 profiles lost their symmetry in y-direction about the origin.

C. DROPLET PATHS

Droplet paths through the instrument were calculated for six droplet diameters between 5 and 200 μm. The diameters correspond to the detection limits of the instrument which covers the most crucial 10–30 μm range of icing particles [28]. We used the CFD solutions of the airflow described in the previous chapter as input for the COMSOL's particle tracing module and droplets were released in the flow before the instrument. In the simulations droplets were independent of each other and no collisions were assumed to happen. At release plane the cross-sectional droplet density of 100 mm^{-2} was used for $\theta = 0°$ and 25 mm^{-2} was used for $\theta > 0°$ angles of attack and droplet velocity was matched with the ambient wind speed. Particle tracing module solved the drag force (5) acting on particles on each time step and updated the velocity and position of the droplets. For each simulation position and velocity of the droplets passing through the yz-plane at $x = 0$ was recorded for analysis. Position and velocity data was used in post processing to solve the droplet number densities ρ in mm^{-3} and finally in terms of relative density ρ/ρ_0.

An example of droplet path calculation is shown for 10 μm droplets in Fig. 4 for 40 m/s ambient wind speed and 10° angle of attack. Only a small proportion of tracked paths near the instrument are shown for clarity with droplet velocity used as color coding.

D. WIND TUNNEL MEASUREMENTS

We validated our simulated droplet concentrations against wind tunnel experiments with icing conditions.

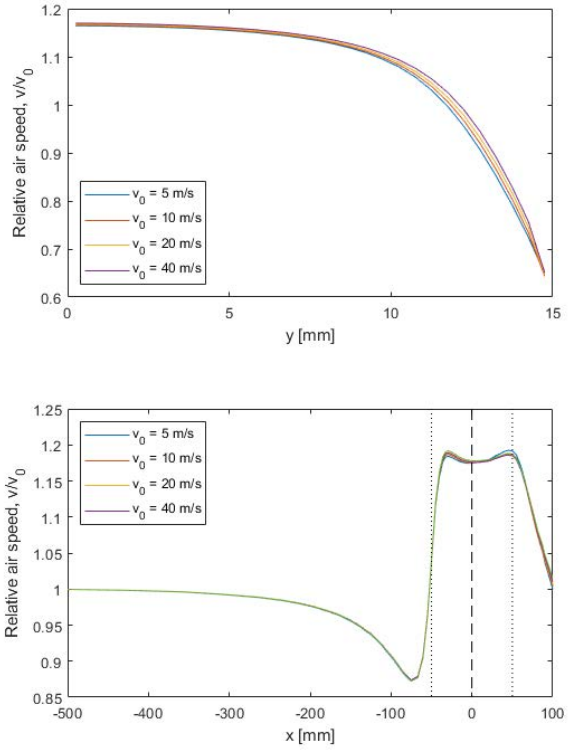

FIGURE 3. Wind speed profiles through the measurement volume along the axis shown in Fig. 2 relative to the wind speed with 0° angle of attack. Dashed line in the lower figure shows the location of measurement volume and dotted lines show the extent of the knife edge air guide. It can be seen that relative wind speed profiles are nearly identical at all simulated ambient wind speeds.

1) Wind tunnel was set to have wind speed $v_0 = 7$ m/s and temperature $T = -5$ °C. Cloud droplet instrument was placed in the wind tunnel and oriented parallel to the airflow. Small water droplets were injected into the airflow and the cloud droplet instrument measured the droplets for a 24-minute period with a 1.5 cm^3/s sampling rate.
2) For the second experiment the angle of attack of the instrument was adjusted to $\theta = 10°$. Wind speed was increased to 10 m/s and 3 minutes of droplet data was measured.

Wind tunnel conditions (speed, temperature, LWC) were stable during the experiments but ambient reference values for droplet concentration and size distribution in the airflow were unavailable. Total water content of the airflow was kept at approximately 0.4 g/m^3 during the experiments. The majority of the detected droplets were smaller than 20 μm in diameter and only a few over 100 μm were observed.

The spatial distribution of the detected droplets in the first experiment with $\theta = 0°$ are shown in Fig. 5 together with the simulated droplet densities. Measured droplets are shown for sizes 10 ± 2 μm, 20 ± 3 μm and 40 ± 10 μm. For larger droplets the size range was increased due to their lower total amount. Spatial distribution of measured and simulated droplet concentrations are in good agreement inside

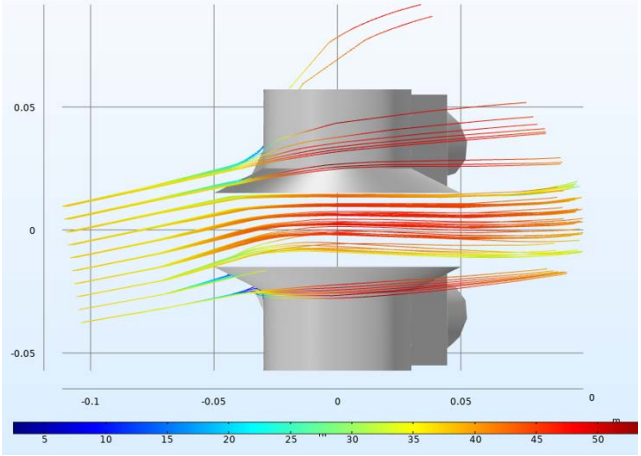

FIGURE 4. A top-down view of the simulated paths of cloud droplets with 10 μm diameter in the non-isoaxial sampling case. Only 100 droplet paths are drawn for clarity. Ambient wind speed and droplet release speed is 40 m/s at a 10° angle of attack. Droplets were released from a grid 0.5 m before the instrument. Droplet speed is used to color the paths.

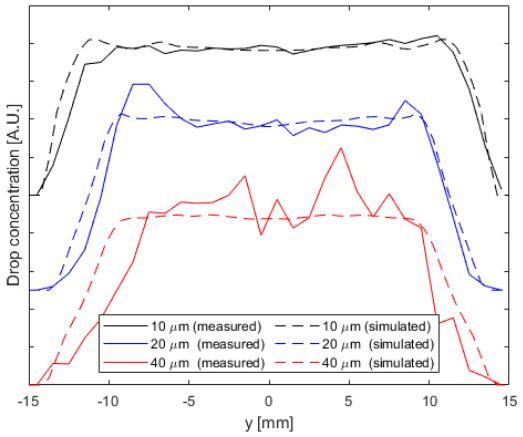

FIGURE 5. Comparison of droplet concentration measurement in a wind tunnel and corresponding simulation for three droplet diameters. Wind speed was 7 m/s and the angle of attack was 0° in both cases. Each concentration profile is normalized by its own sum. Both simulations and measurements are zero on the instrument walls ($|y| = 15$ mm) but offsets are added to 10 μm and 20 μm cases for better visualization.

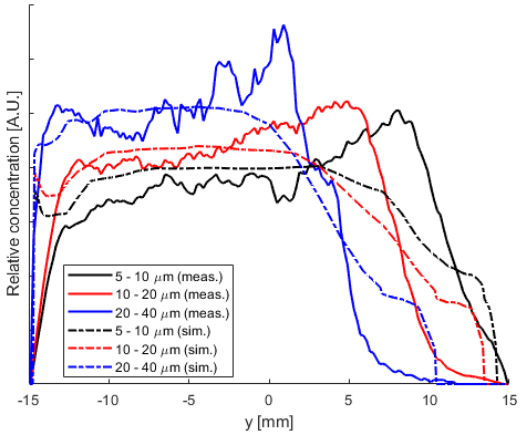

FIGURE 6. Measured and simulated droplet concentrations at ten degree angle of attack of wind for three different droplet intervals.

the measurement volume of the instrument. Additionally, it was possible to solve the velocity of some detected droplets that were observed in two consecutive frames. Observations confirmed that the droplets accelerate when going through the instrument and their velocities matched the simulations.

Results from the second wind tunnel experiment are shown in Fig. 6 for three different droplet intervals in arbitrary units. Simulation results for the intervals are averages of the profiles of the corresponding diameter weighted by the detected number of droplets in the wind tunnel measurements. Due to the angle of attack the line of sight to the measurement volume from the upstream is blocked by the instrument arm above +6 mm coordinates. Measurements and simulations show similar behavior for the shift of the center of mass of the distributions, cutoff positions and increase in concentration as the droplet diameter increases. Differences between measurements and simulations can be seen on how the cutoff happens on the positive y coordinates. Experimental results show steeper cutoff in the droplet density and slight increase of density before the cutoff. It is likely that due to the angle of attack the airflow is time dependent and too complex to be accurately represented in this case by the steady state solution. For our purposes 50 % position of the relative density seems sufficient.

E. RELATIVE DROPLET CONCENTRATION

Summary of the droplet concentrations relative to the ambient concentration at four simulated wind speeds with $\theta = 0°$ are shown in Fig. 7. Concentration profiles are scaled by the average droplet speed at each y-coordinate since the detection probability of the pulsed measurement of the real instrument is proportional to the droplet speed. The concentration profiles of Fig. 7 show that the largest droplets are nearly unaffected by the airflow. Smaller droplets are directed towards the center. Interestingly, it is not necessarily the smallest 5 μm droplets that exhibit the largest sampling effect. For example, the most overestimated case at $v_0 = 5$ m/s wind speed with approximately 10% increase are the 40 μm droplets while at $v_0 = 40$ m/s the most overestimated droplet size is 10 μm with 10% increase in density. Overall all droplets below 200 μm are slightly directed towards the center of measurement volume. The increase in concentration of individual droplet sizes never exceeds 10% of the reference level and the profiles are nearly constant between -10 mm $< y <$ 10 mm and zero on the instrument walls.

Figure 7 shows that the droplet size, wind speed and the measurement volume have an effect on the relation between ambient and measured droplet density. Droplet size and wind speed depend on the environment and can't be changed but the measurement volume can be optimized. Since the instrument can detect the droplet positions, we can filter out droplets that are located in the non-isokinetic region of the measurement volume, i.e. droplets that are too close to the walls. Table 1 shows the expected difference from ambient droplet density averaged over all wind speeds if the detected droplets are filtered by their y-coordinate.

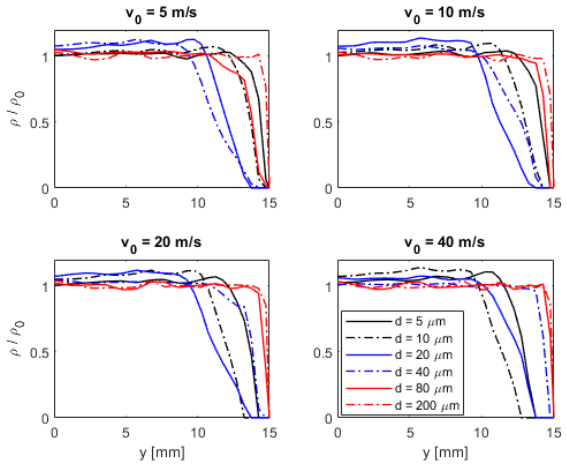

FIGURE 7. Simulated relative droplet concentration profiles in the measurement volume for each droplet size and wind speed. The angle of attack is 0° and only half of the symmetric profiles are plotted from the center ($y = 0$ mm) to the wall ($y = 15$ mm). Droplet concentrations are slightly higher near $y = 0$ mm than in free air and depending on the wind speed and the droplet size the concentration drops rapidly to zero between 8–15 mm distance from the center.

Without filtering, the instrument would underestimate the number of droplets by up -15.4 percent but for some wind speed and droplet diameter combinations the differences can be nearly -20 percent. By limiting the acceptable y coordinates of the measured droplets to two-thirds or one-third of the full measurement range the number of droplets is slightly overestimated but the absolute values of the differences are nearly halved.

A practical compromise to achieve minimal sampling effects and largest measurement volume for the droplet instrument is to reject the droplets that are within a five millimeter distance from the instrument walls. If the measurement volume of the instrument is limited to droplets with $|y| < 10$ mm and if the wind speed data is also available, we can use an approximation for the relative droplet concentration:

$$\frac{\rho}{\rho_0} = 1 + 0.0999 \exp\left(-\frac{(\ln d - \mu(v_0))^2}{2\sigma^2}\right) \qquad (6)$$

Here ρ and ρ_0 are the droplet densities in the measurement volume and in the ambient air respectively, d is the droplet diameter and v_0 is the ambient wind speed. Parameters $\mu(v_0)$ and σ are fitting parameters that can be expressed as $\sigma = 0.6626$ and $\mu(v_0) = -0.48 \ln v_0 + 4.099$. Approximation (6) is based on the simulations and it deviates less than one percent from the simulations for all wind speed v_0 and droplet diameter d combinations used in the simulations. Equation (6) can be used to calibrate the measurement results of this instrument if up to 10 percent overestimation of the droplet concentration is not acceptable. This might be the case if accurate results for LWC, MVD or droplet size distributions are required.

F. DROPLET CONCENTRATION IN NON-ISOAXIAL FLOW

Equation (6) relates the ambient and sampling volume droplet concentrations in isoaxial situation, i.e., when the angle of attack $\theta = 0°$ and the instrument is perfectly aligned with the wind. From Figures 4 and 6 it can be clearly observed that the distributions of the droplet densities along y-axis are asymmetrical when $\theta > 0°$. In principle, the angle of attack of our instrument should remain at 0° since it can rotate and orient itself to the wind. In practice, it is possible that the instrument is not always perfectly aligned. This can happen, for example, if θ is small and the axial torque due to wind is too small to orient the instrument. Other possible reasons for non-isoaxiality could be mechanical misalignment or damaged components or asymmetrical ice accretion on the instrument casing. We used the CFD and particle tracing calculations to study the performance of our instrument in non-isoaxial flow with up to 15° angles of attack.

TABLE 1. Average difference from ambient droplet concentration with different measurement volume limits based on droplet tracing simulations.

Droplet diameter [μm]	Difference to ρ_0		
	Measurement volume y-range		
	full range	$\|y\| < 10$ mm	$\|y\| < 5$ mm
5	-6.1%	+2.5%	+2.1%
10	-10.9%	+6.3%	+5.1%
20	-15.4%	+8.6%	+7.9%
40	-11.7%	+5.2%	+5.6%
80	-4.0%	+1.3%	+1.4%
200	-0.6%	+0.1%	+0.0%

The immediate consequence of the larger than 0° angle of attack is that part of the measurement volume is out of the line of sight from the upstream point of view. Without drag forces there would be a sharp cut-off on the droplet concentration corresponding to the line of sight. Airflow tends to bend parallel to the instrument walls between the instrument arms and drag force (5) changes how the droplets are distributed in the measurement volume. Examples of non-isoaxial simulations are shown for 10° angle of attack in Fig. 8 where relative densities inside the measurement volume are given for droplets in the 5–40 μm range. An increase in the wind speed and angle of attack cause the droplets paths to pass the measurement volume closer to the other wall which leads to asymmetrical density profiles. The Drag force is strong enough to direct the smallest droplets through the gap with relatively small deviation from the perfectly aligned situation. Systematic lack of larger droplets on the other side of the concentration profile may indicate a problem with the orientation capabilities of the instrument.

Angular tolerance and accuracy of the measurement can be improved by limiting the acceptable y-range of the instrument. Figure 9 shows how the perceived droplet density is affected by the measurement volume limits and the angle of attack. The results are averages over all wind speeds with error bars showing the standard deviation. If droplets are accepted from all possible y-coordinates ($|y| < 15$ mm) cloud droplet instrument will always underestimate the number of droplets regardless of their size. Additionally the larger the droplet is, the stronger the effect of the angle of attack. By limiting the measurement volume to $|y| < 10$ mm or even to $|y| < 5$ mm droplet density is much closer to the

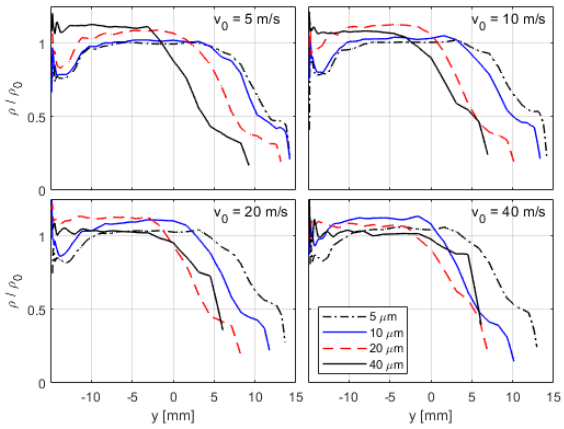

FIGURE 8. Simulation results for relative droplet concentrations at 10 degree angle of attack.

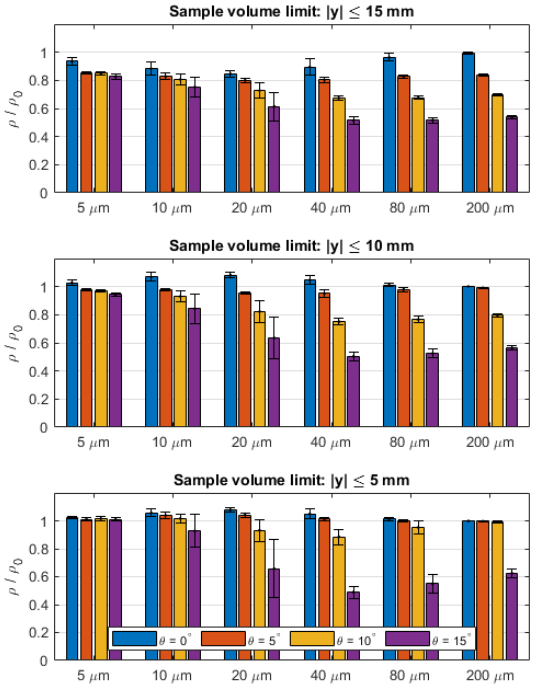

FIGURE 9. Effect of the angle of attack of the instrument and sample volume limit on the relative droplet concentration inside the sample volume. Relative concentrations are averages over the simulated wind speeds between 5 m/s to 40 m/s and the error bars are 1 σ values of the mean. Sample volume limits correspond to full (top) two-thirds (middle) and one-third (bottom) of the full volume.

ambient density and the tolerance for the angle of attack is increased. Larger than 10° angle of attack remains a problem for 20 – 40 μm droplets.

For detecting droplets relevant to icing conditions in 10 μm to 30 μm range, acceptable compromise is to use $|y| <$ 10 mm volume range. Using an even smaller measurement volume further increases the accuracy and tolerance of the instrument but it will increase the measurement time for detecting the same amount of droplets. In practice, knowledge of the available measurement time and the lower limit for the number of detected droplets is to decide how much the measurement volume can be limited. In our instrument the use of a holographic measurement principle allows this choice to be made in the post processing of the raw measurement data.

IV. CONCLUSION

Aerodynamic forces of the airflow within the probe inlet may lead to a non-isokinetic sampling condition and consequently error in the measured values of the particle concentration. The magnitude of the sampling error is a complex combination of the probe design, air speed, particle size, probe inlet orientation as well as the extent and location of the sampling volume within the probed airflow. A novel method to reduce the sampling error of a modestly disturbed particle flow was validated using a holographic cloud droplet imager. It was shown that despite the non-isokinetic conditions accurate droplet density could be obtained

1) by adjusting the location and the size of the sampled volume inside the particle flow and
2) by using a simple algorithm based on the simulated particle trajectories to compensate the redistribution of the particles in the airflow through the measurement volume.

Sampling volume adjustment could be easily realized using the holographic imaging method, which offers multiple well-defined image planes to accurately set the boundaries of the sampling volume even frame by frame.

A combination of CFD solutions and particle tracing was used to study the sampling effects of the holographic cloud droplet imager. The sampling effect on the observed density of 5–200 μm droplets carried by a 5–40 m/s airflow with multiple inlet angles was modelled. Our models were in a good agreement with the data gathered from the wind tunnel experiment. The results show that when the probe inlet was aligned with the airflow the error in droplet density could be kept under 10 % simply by limiting the cross-channel depth of the measurement volume to two thirds of the full wall-to-wall distance of the probe. Likewise using the model-based compensation algorithm the error could be reduced to less than 1 %. Results also indicate that by further limiting the sample volume to cover only one third of the full wall-to-wall distance of the probe inlet droplets up to 40 μm in diameter could be sampled with good accuracy when the angle of the airflow was kept smaller than 10 degrees. Thus compromising between the size of the measurement volume, measurement time and the angular range of the inlet flow reasonable accuracy seems achievable for practical cases. To achieve this it is important to know how the expected combinations of the air speed, probe angle and the droplet size affect the particle distribution in the measurement volume. The applied combination of the CFD and particle tracing seems to offer reliable tool for this. Note also that by combining the information of particle position and density (inherently offered by the holographic imaging method) with the modelling results offers a way to continuously analyze the particle flow and further to determine the best position and size for the sampling volume even frame by frame.

REFERENCES

[1] H. R. Pruppacher and J. D. Klett, *Microphysics of Clouds and Precipitation*, 2nd ed. Amsterdam, The Netherlands: Springer, 2010.
[2] P. K. Wang, *Physics and Dynamics of Clouds and Precipitation*. Cambridge, U.K.: Cambridge Univ. Press, 2013.
[3] *Atmospheric Icing of Structures*, Standard ISO 12494:2017, Mar. 2017.
[4] J. Y. Jin and M. S. Virk, "Study of ice accretion and icing effects on aerodynamic characteristics of DU96 wind turbine blade profile," *Cold Regions Sci. Technol.*, vol. 160, pp. 119–127, Apr. 2019. [Online]. Available: http://www.sciencedirect.com/science/article/pii/S0165232X18304476
[5] M. C. Homola, M. S. Virk, P. J. Nicklasson, and P. A. Sundsbø, "Performance losses due to ice accretion for a 5 MW wind turbine," *Wind Energy*, vol. 15, no. 3, pp. 379–389, 2012. [Online]. Available: https://onlinelibrary.wiley.com/doi/abs/10.1002/we.477
[6] V. Turkia, S. Huttunen, and W. Tomas, *Method for Estimating Wind Turbine Prod. Losses due to Icing* (VTT Technology), no. 114. Helsinki, Finland: VTT Technical Research Centre of Finland, 2013.
[7] S. Lance, C. Brock, D. Rogers, and J. Gordon, "Water droplet calibration of the cloud droplet probe (CDP) and in-flight performance in liquid, ice and mixed-phase clouds during ARCPAC," *Atmospheric Meas. Techn.*, vol. 3, no. 6, pp. 1683–1706, 2010. [Online]. Available: https://www.atmos-meas-tech.net/3/1683/2010/
[8] J. K. Spiegel, P. Zieger, N. Bukowiecki, E. Hammer, E. Weingartner, and W. Eugster, "Evaluating the capabilities and uncertainties of droplet measurements for the fog droplet spectrometer (FM-100)," *Atmos. Meas. Techn.*, vol. 5, no. 9, pp. 2237–2260, 2012. [Online]. Available: https://amt.copernicus.org/articles/5/2237/2012/
[9] R. P. Lawson, D. O'Connor, P. Zmarzly, K. Weaver, B. Baker, Q. Mo, and H. Jonsson, "The 2D-S (stereo) probe: Design and preliminary tests of a new airborne, high-speed, high-resolution particle imaging probe," *J. Atmos. Ocean. Technol.*, vol. 23, no. 11, pp. 1462–1477, Nov. 2006.
[10] J. L. Nowak, M. Mohammadi, and S. P. Malinowski, "Applicability of the VisiSize D30 shadowgraph system for cloud microphysical measurements," *Atmos. Meas. Techn.*, vol. 14, no. 4, pp. 2615–2633, Apr. 2021. [Online]. Available: https://amt.copernicus.org/articles/14/2615/2021/
[11] S. Rydblom and B. Thörnberg, "Liquid water content and droplet sizing shadowgraph measuring system for wind turbine icing detection," *IEEE Sensors J.*, vol. 16, no. 8, pp. 2714–2725, Apr. 2016.
[12] S. Rydblom and B. Thornberg, "Measurement of atmospheric icing and droplets," *IEEE Trans. Instrum. Meas.*, vol. 69, no. 8, pp. 5799–5809, Aug. 2020.
[13] P. Y. Chuang, E. W. Saw, J. D. Small, R. A. Shaw, C. M. Sipperley, G. A. Payne, and W. D. Bachalo, "Airborne phase Doppler interferometry for cloud microphysical measurements," *Aerosol Sci. Technol.*, vol. 42, no. 8, pp. 685–703, Jun. 2008, doi: 10.1080/02786820802232956.
[14] M. S. Kumar, S. R. Chakravarthy, and M. Mathur, "Optimum air turbulence intensity for polydisperse droplet size growth," *Phys. Rev. Fluids*, vol. 4, no. 7, Jul. 2019, Art. no. 074607. 10.1103/PhysRevFluids.4.074607
[15] J. P. Fugal and R. A. Shaw, "Cloud particle size distributions measured with an airborne digital in-line holographic instrument," *Atmos. Meas. Techn.*, vol. 2, no. 1, pp. 259–271, Jun. 2009. [Online]. Available: https://amt.copernicus.org/articles/2/259/2009/
[16] J. Henneberger, J. P. Fugal, O. Stetzer, and U. Lohmann, "HOLIMO II: A digital holographic instrument for ground-based *in situ* observations of microphysical properties of mixed-phase clouds," *Atmos. Meas. Techn.*, vol. 6, no. 11, pp. 2975–2987, Nov. 2013. [Online]. Available: https://www.atmos-meas-tech.net/6/2975/2013/
[17] F. Ramelli, A. Beck, J. Henneberger, and U. Lohmann, "Using a holographic imager on a tethered balloon system for microphysical observations of boundary layer clouds," *Atmos. Meas. Techn.*, vol. 13, no. 2, pp. 925–939, Feb. 2020. [Online]. Available: https://amt.copernicus.org/articles/13/925/2020/
[18] G. Guyot, C. Gourbeyre, G. Febvre, V. Shcherbakov, F. Burnet, J.-C. Dupont, K. Sellegri, and O. Jourdan, "Quantitative evaluation of seven optical sensors for cloud microphysical measurements at the Puy-de-Dóme observatory, France," *Atmos. Meas. Techn.*, vol. 8, no. 10, pp. 4347–4367, Oct. 2015. [Online]. Available: https://amt.copernicus.org/articles/8/4347/2015/
[19] K.-M. Doulgeris, M. Komppula, S. Romakkaniemi, A.-P. Hyvärinen, V.-M. Kerminen, and D. Brus, "*in situ* cloud ground-based measurements in the Finnish sub-arctic: Intercomparison of three cloud spectrometer setups," *Atmos. Meas. Techn.*, vol. 13, no. 9, pp. 5129–5147, Sep. 2020. [Online]. Available: https://amt.copernicus.org/articles/13/5129/2020/
[20] A. Korolev, E. Emery, and K. Creelman, "Modification and tests of particle probe tips to mitigate effects of ice shattering," *J. Atmos. Ocean. Technol.*, vol. 30, no. 4, pp. 690–708, Apr. 2013, doi: 10.1175/JTECH-D-12-00142.1.
[21] H. J. Juttula, V. A. Kaikkonen, and A. J. Mäkynen, "Study of the aerodynamic sampling effects of a holographic cloud droplet instrument," in *Proc. IEEE Int. Instrum. Meas. Technol. Conf.*, Dubrovnik, Croatia, May 2020, pp. 1–5.
[22] V. A. Kaikkonen, D. Ekimov, and A. J. Makynen, "A holographic in-line imaging system for meteorological applications," *IEEE Trans. Instrum. Meas.*, vol. 63, no. 5, pp. 1137–1144, May 2014.
[23] V. A. Kaikkonen, E. O. Molkoselkä, and A. J. Mäkynen, "A rotating holographic imager for stationary cloud droplet and ice crystal measurements," *Opt. Rev.*, vol. 27, no. 2, pp. 205–216, Apr. 2020.
[24] E. O. Molkoselka, V. A. Kaikkonen, and A. J. Makynen, "Measuring atmospheric icing rate in mixed-phase clouds using filtered particle data," *IEEE Trans. Instrum. Meas.*, vol. 70, pp. 1–8, 2021.
[25] J. Garcia-Sucerquia, W. Xu, S. K. Jericho, P. Klages, M. H. Jericho, and H. J. Kreuzer, "Digital in-line holographic microscopy," *Appl. Opt.*, vol. 45, no. 5, pp. 836–850, Feb. 2006. [Online]. Available: http://ao.osa.org/abstract.cfm?URI=ao-45-5-836
[26] D. C. Wilcox, *Turbulence Modeling for CFD*, 2nd ed. DCW Industries, La Cañada, California, CA, USA: 1998.
[27] R. Clift, J. R. Grace, and M. E. Weber, *Bubbles, Drops, and Particles*. Academic Press, New York, NY, USA: 1978.
[28] L. Makkonen, "Analysis of rotating multicylinder data in measuring cloud-droplet size and liquid water content," *J. Atmos. Ocean. Technol.*, vol. 9, pp. 258–263, Jun. 1992.

HARRI J. JUTTULA received the M.Sc. degree in physics from the University of Oulu, Oulu, Finland, in 2009. Currently he is working as a Project Researcher with the Measurement Technology Research Unit, Kajaani, Finland. His research interests include CFD modeling and applications of scattering of light and electromagnetic radiation in industrial, and environmental measurements.

VILLE A. KAIKKONEN was born in Oulu, Finland. He received the M.Sc. (Tech.) degree in electrical engineering from the University of Oulu, Oulu, in 2010, where he is currently pursuing the D.Sc. (Tech.) degree in photonics. He has been a Project Researcher with the Measurement Technology Research Unit, Kajaani, Finland, since 2010. His current research interest includes digital holographic imaging, especially in environmental measurement applications.

EERO O. MOLKOSELKÄ received the M.Sc. (Tech.) degree in computer science and engineering from the University of Oulu, Oulu, Finland, in 2019. He is currently pursuing the D.Sc. (Tech.) degree in electrical engineering. His research interests include digital signal processing methods in environmental and industrial measurement applications.

ANSSI J. MÄKYNEN received the M.Sc. (Tech.) (Hons.) and D.Sc. (Tech.) degrees from the University of Oulu, Oulu, Finland, in 1987 and 2000, respectively. He is a Senior Research Fellow and a Research Group Leader with the Faculty of Information Technology and Electrical Engineering, University of Oulu. His current research interest includes optical methods for industrial and environmental on-line inspection, especially characterization of materials using various imaging and spectroscopic methods.